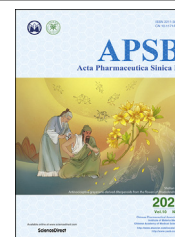




Chinese Pharmaceutical Association
Institute of Materia Medica, Chinese Academy of Medical Sciences

Acta Pharmaceutica Sinica B

www.elsevier.com/locate/apsb
www.sciencedirect.com



ORIGINAL ARTICLE

20(S)-Protopanaxatriol promotes the binding of P53 and DNA to regulate the antitumor network via multiomic analysis



Zhihua Wang^a, Wenbo Wu^a, Xiangchen Guan^a, Shuang Guo^a,
Chaowen Li^a, Ruixue Niu^a, Jie Gao^a, Min Jiang^a, Liping Bai^b,
Elaine Laihan Leung^b, Yuanyuan Hou^{a,*}, Zhihong Jiang^{b,*}, Gang Bai^{a,*}

^aState Key Laboratory of Medicinal Chemical Biology, College of Pharmacy and Tianjin Key Laboratory of Molecular Drug Research, Nankai University, Tianjin 300353, China

^bState Key Laboratory of Quality Research in Chinese Medicine, Macau University of Science and Technology, Taipa, Macau, China

Received 14 September 2019; received in revised form 2 December 2019; accepted 6 December 2019

KEY WORDS

Multiomics analysis;
P53;
20(S)-Protopanaxatriol;
DNA binding;
Ginsenosides anti-tumor
network

Abstract Although the tumor suppressor P53 is known to regulate a broad network of signaling pathways, it is still unclear how certain drugs influence these P53 signaling networks. Here, we used a comprehensive single-cell multiomics view of the effects of ginsenosides on cancer cells. Transcriptome and proteome profiling revealed that the antitumor activity of ginsenosides is closely associated with P53 protein. A miRNA–proteome interaction network revealed that P53 controlled the transcription of at least 38 proteins, and proteome-metabolome profiling analysis revealed that P53 regulated proteins involved in nucleotide metabolism, amino acid metabolism and “Warburg effect”. The results of integrative multiomics analysis revealed P53 protein as a potential key target that influences the anti-tumor activity of ginsenosides. Furthermore, by applying affinity mass spectrometry (MS) screening and surface plasmon resonance fragment library screening, we confirmed that 20(S)-protopanaxatriol directly targeted adjacent regions of the P53 DNA-binding pocket and promoted the stability of P53–DNA interactions, which further induced a series of omics changes.

© 2020 Chinese Pharmaceutical Association and Institute of Materia Medica, Chinese Academy of Medical Sciences. Production and hosting by Elsevier B.V. This is an open access article under the CC BY-NC-ND license (<http://creativecommons.org/licenses/by-nc-nd/4.0/>).

*Corresponding authors.

E-mail addresses: houyy@nankai.edu.cn (Yuanyuan Hou), zhjiang@must.edu.mo (Zhihong Jiang), gangbai@nankai.edu.cn (Gang Bai).

Peer review under responsibility of Chinese Pharmaceutical Association and Institute of Materia Medica, Chinese Academy of Medical Sciences.

<https://doi.org/10.1016/j.apsb.2020.01.017>

2211-3835 © 2020 Chinese Pharmaceutical Association and Institute of Materia Medica, Chinese Academy of Medical Sciences. Production and hosting by Elsevier B.V. This is an open access article under the CC BY-NC-ND license (<http://creativecommons.org/licenses/by-nc-nd/4.0/>).

1. Introduction

The *TP53* tumor suppressor gene has been identified for 40 year¹. As one of the most important cancer cell regulatory transcription factors, the P53 protein plays a wide regulatory role in gene expression, DNA repair, metabolism, cell survival, cell cycle arrest, apoptosis, and senescence^{2–4}. Various studies have shown that P53 controls a broad and flexible network in many fields, such as in transcriptome, as a superior transcription factor, P53 remodeling the miRNA–mRNA interaction network in miRNA loading onto AGO2⁵; P53 interaction to miRNA-34b/c induce the polymorphisms on the risk of osteoporosis⁶; the expression levels of miR-21, miR-34a, miR-125b, miR-648 and miR-181d in primary glioblastoma patients are levels inversely correlate with P53 and MGMT⁷, etc. P53 simultaneously regulates the functions of several proteins, including overexpression of the P53 repressor MDM2⁸; transcriptional activation of the P21 cyclin-dependent kinase inhibitor gene⁹; induction of the pro-apoptotic BCL-2 family members, and facilitation of caspase activation and cell death¹⁰. Moreover, many studies have shown that the transformation of tumor cell energy metabolism is regulated by P53, including the “Warburg effect” metabolism^{11,12}. Although these studies add greatly to our understanding of the underlying mechanisms of P53, there is little research regarding the systematic regulation of P53 under the influence of drugs. In particular, there are few studies that report a comprehensive analysis of P53 in the host gene–mRNA–miRNA–protein–metabolite system interaction network. Furthermore, the few reports regarding this subject are partially contradictory^{13,14}.

Ginsenosides, the active constituents of ginseng, a traditional Chinese medicine, have been demonstrated to be effective in treating several types of cancer diseases^{15,16}. However, the traditional usage of ginseng often involves multiple ingredients of various herbs, and as such, the mechanism of action of ginseng is obscure and difficult to discern^{17,18}. The specific ginsenoside component that interacts with host protein(s) for cancer treatment remains unknown. Although we have previously identified RAS proteins as potential targets of ginsenosides *via* proteomic and bioinformatic techniques¹⁹, the role of these proteins in gene transcription, protein translation, protein expression regulation, and metabolic pathways of the overall host cell has not been investigated.

Therefore, the purpose of our study was to create a comprehensive overview of the global P53 regulation network underlying the anti-tumor effects of ginsenosides, with a particular focus on P53 DNA-binding functions. We performed multiomic analyses on the non-small cell lung cancer cell line A549 treated with ginsenosides. The mRNA and miRNA of the transcriptome, proteomics, and phosphoproteomics of the proteome, and the metabolome in positive and negative mode were analyzed together. Correlation of transcriptome and proteome profiling revealed the functional pathways and critical genes and proteins involved in the anti-tumor activity of ginsenosides. The integrated miRNA with proteome analysis revealed the transcription mechanism of the regulation interaction network by key proteins. Proteome–metabolite interaction analysis identified the proteins driving the metabolism pathways. Together, the results from the multiomics analyses summarized the core target protein underlying the anti-tumor effects of ginsenosides. Furthermore, affinity mass spectrometry (MS) screening and surface plasmon resonance fragment library screening combined with fluorescence polarization technology were used to study the active ingredients of

ginsenosides and the interaction mechanism of the candidate ligands with P53.

2. Materials and method

2.1. Cell lines and cell culture conditions

The human non-small cell lung cancer cell line A549 was obtained from Procell Life Science & Technology Co., Ltd. (Wuhan, China) with an STR identification report (Supporting Information Fig. S1). A549 cells were cultured in Ham's F-12K media containing 10% FBS, 10 mg/mL streptomycin, and 10 mg/mL penicillin (GE Healthcare Life Sciences, Logan, UT, USA) at 37 °C with 5% CO₂. A549 cells were passaged or harvested by incubation with 1× TrypLE Express (Life Technologies, Grand Island, NY, USA) at 37 °C for 2 and 5 min.

2.2. Preparation of the omics cell model

For the omics model, A549 cells were used for cluster experiments after three generations of resuscitation. After growing A549 cells at 37 °C for 12 h, 0.25 mg/mL ginsenosides (the IC₅₀ of the total ginsenoside inhibition cell viability of A549, Supporting Information Fig. S2A and S2B) or vehicle control (0.1% DMSO) were added to each well, and the cells were continue cultured for another 12 h. For the transcriptome analysis of RNA and miRNA sequencing, the cell count was above 2×10^5 per sample. The cells were cultured in a 6-well plate, and experiments were reproduced at least in triplicate for the control and sample groups. The proteomic and phosphoproteomic experiments were performed with at least 2×10^7 cells per sample. The cells were cultured in 150-cm² plates, with two plates for one group, and the experiments were reproduced at least in triplicate for the control and sample groups. In the metabolome experiments, cells were above 1×10^7 for per sample. Cells were cultured in 150-cm² plates and reproduced at least in sextuplicate for the control and sample groups. All of the cells were counted using the Bio-Rad TC20™ (Bio-Rad, Hercules, CA, USA) automated cell counter.

2.3. Total RNA extraction

Total RNA was extracted from collected cells using Trizol (Invitrogen, Carlsbad, CA, USA). We added 1×10^6 cells to 1 mL of Trizol according to the manufacturer's instructions. Cells were homogenized for 2 min and then allowed to rest horizontally for 5 min. The mix was centrifuged at 12,000×g for 5 min at 4 °C. Then the supernatant was transferred into a new EP tube with 0.3 mL of chloroform/isoamyl alcohol (24:1), mixed vigorously for 15 s, and then centrifuged at 12,000×g (Mikro220R, Hettich, Tuttlingen, Germany) for 10 min at 4 °C. After centrifugation, the upper aqueous phase, which included the RNA, was transferred into a new tube with an equal volume of isopropyl alcohol and then centrifuged at 13,600 rpm (Mikro220R, Hettich, Tuttlingen, Germany) for 20 min at 4 °C. After discarding the supernatant, the RNA pellet was washed twice with 1 mL of 75% ethanol, centrifuged at 13,600 rpm (Mikro220R) for 3 min at 4 °C to collect residual ethanol, and then air dried for approximately 5–10 min in the biosafety cabinet. Finally, approximately 25–100 μL of DEPC-treated water was added to dissolve the RNA. The quality and concentration of the total RNA were

assessed using an Agilent NanoDrop 2100 Bioanalyzer (Thermo Fisher Scientific, Waltham, MA, USA).

2.4. miRNA library construction

The library was prepared using 1 µg of total RNA for each sample. Total RNA was purified by electrophoretic separation on a 15% urea denaturing polyacrylamide gel *via* electrophoresis, and the small RNA regions corresponding to the approximately 18–30 nt bands in the marker lane (14–30 ssRNA Ladder Marker, TAKARA, Dalian, China) were excised and recovered. The recovered small RNAs were then ligated to a 5'-adaptor and a 3'-adaptor. The adapter-ligated small RNAs were subsequently transcribed into cDNA by SuperScript II Reverse Transcriptase (Invitrogen, Karlsruhe, Germany), and then several rounds of PCR amplification with PCR Primer Cocktail and PCR Mix were performed to enrich the cDNA fragments. The PCR products were selected by agarose gel electrophoresis, with the target fragments being approximately 100–120 bp, and then purified by a QIAquick Gel Extraction Kit (QIAGEN, Valencia, CA, USA). The quality and concentration of the library was assessed *via* two methods: 1) the distribution of the fragment sizes was assessed using an Agilent 2100 Bioanalyzer, 2) and the library was quantified using real-time quantitative PCR (QPCR, TaqMan Probe). The final ligation PCR products were sequenced using the BGISEQ-500 platform (BGI, Shenzhen, China).

2.5. Metabolome experimental procedures

Total metabolites were extracted from each group using approximately 1×10^7 cells in 1 mL of methanolic acetonitrile aqueous solution (2:2:1, *v/v/v*). The cells were then vortexed for 60 s, incubated at for 30 min twice, and then the protein was placed at -20°C for 1 h. The solution was centrifuged at 14,000 rcf for 20 min at 4°C , and then the supernatant was stored at -80°C until future use. Samples were separated on an Agilent 1290 Infinity LC Ultra-High-Performance Liquid Chromatography System (Agilent Technologies, CA, USA) using a HILIC column. The column temperature was 25°C , and the flow rate was 0.3 mL/min. The mobile phase of composition A was water+25 mmol/L ammonium acetate+25 mmol/L ammonia, and B was acetonitrile. The gradient elution procedure was as follows: approximately 0–1 min, 95% B; approximately 1–14 min, B varied linearly from 95% to 65%; approximately 14–16 min, B changed linearly from 65% to 40%; approximately 16–18 min, B was maintained at 40%; approximately 18–18.1 min, B changed linearly from 40% to 95%; approximately 18.1–23 min, B was maintained at 95%. The sample was placed in a 4°C autosampler. In order to avoid the effects of instrument detection signal fluctuations, continuous analysis of samples was performed in random order. QC samples were inserted into the sample queue to monitor and evaluate the stability of the system and the reliability of the experimental data. Electrospray ionization (ESI) positive and negative ion modes were used for detection. The sample was separated by UHPLC and subjected to mass spectrometry using a TripleTOF 5600 mass spectrometer (AB SCIEX, Framingham, MA, USA). The ESI source conditions after HILIC chromatographic separation were as follows: ion source gas 1 (gas 1): 60; ion source gas 2 (gas 2): 60; curtain gas (CUR): 30; source temperature: 600°C ; ion spray voltage floating (ISVF) ± 5500 V (positive and negative modes); TOF MS scan *m/z* range: approximately 60–1000 Da; product ion

scan *m/z* range: approximately 25–1000 Da; TOF MS scan accumulation time 0.20 s/spectra; and product ion scan accumulation time 0.05 s/spectra. Secondary MS was obtained using information-dependent acquisition (IDA) and high sensitivity mode, with a declustering potential (DP): ± 60 V (both positive and negative modes), collision energy: 35 ± 15 eV, and IDA settings were as follows: exclude isotopes within 4 Da; and candidate ions to monitor per cycle: 6. The raw data were converted to mzXML format by ProteoWizard, and then the XCMS program was used for peak alignment, retention time correction, and peak area extraction. Metabolite structure identification used a method of accurate mass matching (<25 ppm) and secondary spectral matched against in-house tandem MS spectral library (Shanghai Applied Protein Technology, Shanghai, China). Overall, The MS/MS spectra matching score was calculated using dot-product algorithm, which take the fragments and intensities into consideration. The matching score cutoff was set as 0.8. The MS/MS spectra matching results were confirmed with standards. For the data extracted by the XCMS, the ion peaks with a sum of $>2/3$ were deleted. The application software SIMCA-P 14.1 (Umetrics, Umea, Sweden) was used for pattern recognition. The data were preprocessed by Pareto-scaling for multidimensional statistical analysis, including unsupervised principal component analysis (PCA) analysis, supervised partial least squares discriminant analysis (PLS-DA), and orthogonal partial least squares discriminant analysis (OPLS-DA). The variable expression weight of the metabolites (VIP) is used to measure the influence intensity and interpretation ability of each metabolite expression pattern on the classification and discrimination of each group of samples, and to explore biologically significant differential metabolites. Metabolites with both multidimensional statistical analysis $\text{VIP} > 1$ and univariate statistical analysis P value < 0.01 were selected as metabolites with significant differences. Univariate statistical analysis was further used to verify whether the differential metabolites were significant. Single-dimensional statistical analysis included Student's *t* test and variation multiple analysis. R software created the volcano maps. Data access the high-throughput metabolome data from this study have been submitted to the Metabolomics Workbench as an attachment file (<https://doi.org/10.21228/M8WD6C>) with the Project ID PR000803 and study ID ST001191. We thank APTBIO (Shanghai, China) for technical supports and deep discussion.

2.6. Bioinformatics analysis

In this part, the gene ontology annotation (GOA) database (<http://www.ebi.ac.uk/GOA/>) provided gene ontology (GO) annotations to RNA from RNACentral, proteins in the UniProtKB. The Uniprot ID mapping (<https://www.uniprot.org/uploadlists/>) is used to provide name conversion for various types of omics databases. The DIANA-web server 5.0²⁰ (<http://diana.imis.athena-innovation.gr/DianaTools/index.php?r=site/page&view=software>) provides us with complete algorithms, databases and software for analysis of expression regulation and annotation of small RNAs. The KEGG Mapper (https://www.genome.jp/kegg/tool/map_pathway2.html) and CluoGO²¹ in Cytoscape were applied to verify the significance enriched signal pathway. Human Protein–Protein Interaction Prediction²² and STRING²³, functional protein association networks (<https://string-db.org/>) were used for protein–protein interaction (PPI) analysis. The OmicsNet²⁴ (<https://www.omicsnet.ca/OmicsNet/>) was used to supports integrative analysis of multiple lists of different types of molecules

interactions: protein–protein, TF–gene, miRNA–gene and metabolite–protein. Then, all differentially expressed omics data were input into corresponding feature online tools or offline softwares for bioinformatics analysis. Finally, these analytical data are exported in different ways and then imported into Cytoscape 3.7.1²⁵ (<https://cytoscape.org/>) for unified visual network analysis.

2.7. Correlation analysis of mRNA and protein data

To compare the differentially regulated genes and proteins observed in mRNA and proteomics, respectively, we used a nine-quadrant map to correlate the data. We first converted the ID names to the Uniprot ID mapping for differentially expressed genes and proteins in the transcriptome and proteomic data (unified with UniprotKB Gene name). Then we imported the transcriptome and proteomic data into the online software Omicsshare (<http://www.Omicshare.com/tools/Home/Soft/jxx>), and the parameters were set. The default transcriptome was set to identify mRNA that was upregulated and downregulated 2-fold, and the proteomic data were set to identify proteins that were upregulated and downregulated 1.2-fold. This program also allowed the data to be customized to account for the multiple differences in each group. The color of each quadrant was selected by default. The title of the *x*- and *y*-axes was defined without the use of Chinese or special characters in the name of either axis. The data processing results were received in approximately 3 min. The output file contained: 1) A-VS-B.annot.all.xls: a nine-quadrant summary table that recorded the quadrant information of all genes/proteins, the expression levels in the transcriptome and proteome, and functional annotations; 2) A-VS-B_1 (2, 3, 4 ...).annot.xls: each quadrant sub-table (9), which recorded the gene/protein information of each quadrant, the expression level in the transcriptome and the proteome, and function comments; and 3) A-VS-B.associate.png/pdf: nine-quadrant results. The nine-quadrant map was divided into nine quadrants, where the ordinate represented the \log_2 value of the ploidy gene differential multiple, and the abscissa represented the \log_2 value of the protein expression difference multiple. Genes that were upregulated at least 2-fold were considered significantly different genes ($\log_2 = 1$ or -1), and proteins that were upregulated at least 1.2-fold were considered significantly different proteins ($\log_2 = 0.263$, or -0.263). Specifically, quadrant 5 indicated the co-expressed mRNA and protein that were not differentially expressed; quadrants 3 and 7 indicated the mRNA that was consistent with the corresponding differential protein expression pattern; quadrants 1, 2, and 4 indicated the proteins that were expressed higher than the mRNA; quadrant 6, 8, and 9 indicated the proteins that were expressed lower than mRNA. A Venn diagram was used to show the logical connections between different groups (collections). Finally, these associated data were again analyzed *via* bioinformatics as described above.

2.8. Comparative network-based analysis of protein and miRNA data

In order to further explain the influence of ginsenosides in the transcription and translation process, we correlated the miRNAs and proteomes after ginsenoside interference. First, the TargetScanHuman 7.2²⁶ (http://www.targetscan.org/vert_72/) online tool was used to search for theoretical target protein regulatory miRNAs. As a results, the 73 protein names

associated with the proteogenomic analysis were matched with 255 mirbase IDs. When a protein was mapped to multiple miRNA subtypes, we selected the miRNA that showed the greatest correlation. Then, the detected 727 differentially expressed miRNAs were correlated with protein-transformed 255 theoretical miRNAs. The *P*-value was used to perform a significance test and further calculate the *P*-value of the FDR. When the FDR <0.01, the miRNA and protein pairs were considered to have a significant correlation between log-fold changes in miRNA and protein. The GO enrichment and KEGG pathway analyses were then performed on these associated miRNAs and proteins using the DIANA-web server 5.0 and KEGG Mapper, as previously described. Finally, the analysis results were then imported into Cytoscape for visual analysis.

2.9. Comparative network-based analysis of protein and metabolite data

In this study, we converted the differential substances detected by metabolomics into KEGG object identifier and converted them into KEGG IDs. To create an integrated network for visualization and analysis, we use the MetaboAnalyst²⁷ (<http://www.metaboanalyst.ca/>) online tool for correlation analysis. In the web search page, genes or metabolites were imported into the appropriate “gene list” or “metabolite list” box, the upload data type was specified by clicking the drop-down menu next to “ID Type” and selecting the “metabolites-genes” (official human gene symbol ID for proteins and KEGG ID for metabolites). Then the data automatically corresponded to the respective data frame. We continued to click the “submit” button in order to receive the corresponding data set for each step. We then clicked the download result link to directly export the corresponding data set. The default view of the data was mapped to the KEGG Global Metabolism Network. We also input these data into Cytoscape for visualization network analysis.

2.10. Multiomics global regulation interaction network analysis

The multiomics global regulation interaction network analysis of the anti-tumor activity of ginsenosides was performed by OmicsNet (<https://www.omicsnet.ca/OmicsNet/>). In the OmicsNet homepage, there are six panels corresponding to six different input types: Genes/Proteins, Transcription factors, miRNAs, Metabolites, Microbiome, and Graph file. For this study, significance differential expression Genes/Proteins, Transcription factors, miRNAs and Metabolites were co-analysis according to the web page tutorials. Briefly, copy-and-paste the list of Genes or Proteins, miRNAs and Metabolites into the box of “Gene List”, “miRNA List”, or “Metabolite List”, respectively. Then click the dropdown menu next to “ID Type” to specify the type of data uploading (official human gene symbol ID for proteins, miRBase ID for miRNAs, and KEGG ID for metabolites), and click “Yes” to continue. Then, the data are automatically pasted into their respective boxes, and click the “Submit” button. After a few seconds, we received a network association graph. It included PPIs, transcription factor–gene interactions, miRNA–gene interactions, and metabolite–protein interactions, which also included a comprehensive analysis of molecular functions and signaling pathways. We downloaded the images directly and uploaded the raw data into Cytoscape for image editing and arranging.

2.11. P53 wild type and mutation protein expression and purification

All wild-type and mutant P53 recombinant plasmids are derived from GENEWIZ Co., Ltd. (Suzhou, China). The protein sequence of P53 DNA-binding core region 94-312aa contains 657 bases optimized to better express proteins in *Escherichia coli*. Protein expression and purification steps refer to previously studied methods^{28,29}. Briefly, the P53 wild-type gene and the mutant gene were cloned into the pET-28a expression vector, and the 6× his tag was fused at the C-terminus. The expression vector was transformed with *E. coli* BL21 (DE3) strain and induced with 200 mmol/L of isopropyl β-D-1-thiogalactoside (IPTG) at an optical density at 600 nm of 0.6. After 16 °C overnight expression, the cultured protein-expressing cells were collected in a buffer consisting of 20 mmol/L Tris HCl (pH 8.0), 500 mmol/L NaCl and 5% glycerol, and stored at -80 °C until use. When purifying the protein, the collected expression cells were taken out, and after completely dissolving, the cells were disrupted by an ultrasonic apparatus for 1 h, and the time interval was stopped for 1 s every 3 s, and the cycle is repeated. After the completion of the ultrasound, centrifugation at 13,000×g for 15 min at 4 °C. The supernatant was applied to a Ni-NTA column for affinity adsorption. Washing with a buffer containing 40 mmol/L imidazole, 20 mmol/L Tris-HCl (pH 8.0), 500 mmol/L NaCl and 5% glycerol, eluting with a buffer containing 400 mmol/L imidazole, 20 mmol/L Tris-HCl (pH 8.0), 500 mmol/L NaCl and 5% glycerol. Protein purification was then performed on a Akta protein purification system using a superdex 200 increase 10/300 GL molecular sieve column (GE Healthcare Bio-sciences, uppsala, Sweden, [Supporting Information Fig. S3A](#)). Finally, according to SDS-PAGE analysis, the purified P53 wild-type and mutant proteins were all >95% pure for using ([Fig. S3B](#)).

2.12. Affinity MS screening active compounds from total ginsenosides extracts

The specific experimental procedure for affinity MS screening has been previously reported^{30,31}. Concisely, we will react the purified protein and the crude ginsenoside extract in a certain proportion (50 μmol/L protein: 0.2 mg/mL ginseng total saponin), and then remove the small molecules that are not reacted with the protein by ultrafiltration. The protein and small molecule complexes are then dissociated and detected by MS. We define the affinity index (AI) as the ratio of the MS response of the compound detected in the target to the MS response of the control sample. The values of each group are exported from the Masslynx 4.1 analysis software and manually calculated in the Excel table. The initial screening compound was selected according to the rules of the average of AI>2, RSD<30% and *P* < 0.05 for three replicates.

2.13. The surface plasmon resonance (SPR) assay

In this study, fragment library screening and K_D measurements were performed using a Biacore T200 optical biosensor (GE Healthcare). The S series CM5 sensor chip (GE Healthcare) was used to couple the target protein, and the running buffer was PBS with 5% DMSO. The recombinant P53 wild-type and mutant proteins (about 50 mg/mL) were coupled to a CM5 chip with approximately 7000 RU coupling amount for each channel. Proteins were diluted with 10 mmol/L sodium acetate buffer (pH 5.0). In the molecular fragment library screening, each compound concentration was diluted to 100 μmol/L in a 96-well measuring

plate, sequentially passed through the coupled CM5 chip, and then the data was recorded and stored. For evaluation of the K_D value, each compound was diluted 11 times from 500 to 0.488 μmol/L, sequentially passed through the chip from low concentration to high concentration, and then the data were recorded and saved in real time. The molecular effects of non-specific binding and signal drifts were removed using molecular weight adjustment and solvent correction. All data processing was performed in the Biacore T200 analysis software.

2.14. Molecular docking and sequence alignment

To accurately reflect the interaction between the protein and the compound, we found the crystal structure of the P53 protein (PDB code: 4AGL¹¹ and 6FJ5³²) from the research collaboration for structural bioinformatics (RCSB). The molecular docking was performed using Schrödinger version 2015-4³³. Firstly, we input the crystal structure of P53 protein into the software for dehydration, hydrogenation, charge and other pretreatment, and then determine the binding sites to form lattice pockets. Subsequently, the input compound is subjected to hydrogenation, charge treatment or the like to form a stereoscopic conformation. Finally, elaborate molecular docking analysis of compounds and P53 was performed both standard precision (SP) and extra precision (XP) glide mode docking. The final result was shown as a cartoon or energy diagram by pymol. The homologous sequence alignment of the proteins was performed using clusalw and the final map was obtained from Esript 3.0³⁴.

2.15. DNA probe synthesis

In this study, 10-segment-specific DNA sequences were derived from differential miRNAs detected by transcriptomics: hsa-miR-144-3p (5'-TACAGTATAGATGATGTACT-3'), hsa-miR-153-3p (5'-TTGCATAGTCACAAAAGTGATC-3'), hsa-miR-760 (5'-CGGCTCTGGGTCTGTGGGGA-3'), hsa-miR-195-5p (5'-TAGCAGCACAGAAATATTGGC-3'), hsa-miR-142-5p (5'-CATAAAGTAGAAAGCACTACT-3'), hsa-miR-186-5p (5'-CAAAGAAT TCTCCTTTTGGGCT-3'), hsa-miR-34c-5p (5'-AGGCAGTGTA GTTAGCTGATTGC-3'), hsa-miR-493-5p (5'-TTGTACATG GTAGGCTTTCATT-3'), hsa-miR-155-5p (5'-TTAATGCTAATC GTGATAGGGGTT-3') and hsa-miR-485-5p (5'-AGAGGC TGGCCGTGATGAATTC-3'). Then the carboxyfluorescein was to the 5' terminus of all of the above sequences. Gene synthesis and fluorescein labeling were completed by GENEWIZ Co., Ltd. (Suzhou, China).

2.16. Fluorescence polarization (FP) assay

The FP assay was conducted on a TECAN Spark 10M (Tecan, Mannedorf, Switzerland). In order to explore the binding of the DNA fluorescent probe to the P53 protein, we diluted the protein concentration 11 times from 200 μmol/L to 0 with FP buffer (10 mmol/L MgCl₂, 200 mmol/L NaCl, 20 mmol/L Tris-HCl, 5 mmol/L DTT, pH 8.0) and then mixed the 50 nmol/L probe (final concentration) to each concentration point. In the PPT experiment, we fixed the protein concentration at 10 μmol/L and the probe concentration at 50 nmol/L. We then diluted the PPT concentration 10 times from 500 μmol/L to 0. The fluorescence polarization value was read on the TECAN Spark 10M (excitation wavelength 485 nm, the emission wavelength 525 nm). The

experiment was repeated three times for each concentration, and the EC₅₀s were determined using GraphPad Prism 5.

2.17. Quantification and statistical analysis

For a detailed analysis of statistical results, please see each individual method. The frequently occurring *P*-values in this report were calculated by a two-tailed Student's *t* test. It represents a significant difference in the sample, generally $P < 0.05$ was significant and $P < 0.01$ was very significant, which means that the probability of the difference between the samples caused by the sampling error is less than 0.05 or 0.01. Relative standard deviation (RSD) is used to indicate the precision of the analytical test results. The smaller the value, the better the repeatability. False discovery rate (FDR) is the expected value of the number of false rejections [rejecting the true (original) hypothesis] as a percentage of all rejected hypotheses. As a control indicator for the hypothesis test error rate, the control value can be selected according to needs, and the value of the traditional hypothesis test is usually set to 0.05. In this study, all biochemical analyses were performed at least three times independently. Data were analyzed using GraphPad Prism 5.0. For the correlation analyses, Pearson's correlation was used for measurement of a linear correlation in the data. The volcano map was used to show the results of the differential expression analysis, and the Venn diagram was used to show the logical connections between different groups (collections). GO enrichment analysis and KEGG pathway analysis were performed based on online tools, such as KEGG mapper and string, and offline tools, such as Cytoscape 3.7. Other non-computational analyses were performed using Excel (Microsoft Excel 2016).

Additional data analysis methods are shown in the [Supporting Information](#).

3. Results

3.1. Integrated transcriptome, proteome, and metabolome analyses

In this study, we performed multiomics analyses on the non-small cell lung cancer cell line A549 treated with ginsenosides (Fig. 1A). To acquire a comprehensive view of the omics processes in cells influenced by ginsenosides, A549 were treated with 0.25 mg/mL ginsenoside extract for 12 h, and control cells received 0.1% DMSO. RNA sequencing and miRNA sequencing on the total transcriptome was performed, while proteomic and phosphoproteomic differential expression in the total proteome was analyzed, and the total metabolome was analyzed. The transcriptome, proteome, and metabolome profiles were visualized in a correlation heatmap by Pearson's correlation, which represented a biological duplication of each sample data (Figs. S2C–E). Overall, the data from all three omics groups were highly reproducible with >95% between biological replicates and a correlation coefficient of >85% across all samples. Altogether, 21,350 unique Entrez gene IDs were mapped to transcripts, 4544 miRNAs were detected, 5499 proteins were identified from 33,779 peptides, and 9135 modification sites were detected in 4820 modified phosphopeptides, and 4047 spectra in positive MS mode and 3058 spectra in negative MS mode were detected in the metabolome (Supporting Information Table S1). After correcting for multiple testing by setting the *P*-value at 0.01 and false discovery rate (FDR) at 0.05, 934 genes (327 downregulated and 607 upregulated), 727 miRNA (183 downregulated

and 544 upregulated), 454 proteins (190 downregulated and 264 upregulated), and 459 dysregulated modified phosphorylation sites (180 downregulated and 279 upregulated) were detected. Furthermore, 67 compounds (47 upregulated and 20 downregulated) in positive MS mode and 73 compounds (41 upregulated and 32 downregulated) in negative MS mode were identified as significantly different (Fig. 1B and C).

3.2. Transcriptome and proteome profiling revealed that the antitumor activity of ginsenosides is closely associated with P53

In order to clarify the main biological functions and target proteins of ginsenosides in the A549 cell model, we performed KEGG pathway analysis and PPI network analysis of the detected differential genes and proteins. In order to identify genes consistently, we used the gene names (official gene symbol) of the upregulated or downregulated gene or protein in both omics layers. KEGG pathway analysis indicated that the major regulating pathways in both the transcriptome and proteome were involved in cancer signaling, including the PI3K–AKT, MAPK, RAS, and P53 signaling pathways (Fig. 2A–C). Furthermore, the correlation analysis of the transcriptome and proteome showed that 73 entities were co-regulated in both the transcriptome and proteome (20 co-regulated by transcriptomics and proteomics, 15 co-regulated by transcriptomics and phosphoproteomics, and 38 co-regulated by all three omics; Fig. 2D and E), and the specific 73 co-regulated entities are shown in [Supporting Information Fig. S4](#).

KEGG pathway analysis of the co-regulated entities was demonstrated to be part of several signaling pathways, including the P53 signaling pathway, RAS signaling pathway, MAPK signaling pathway, miRNAs in cancer, and PI3K–AKT signaling pathway (Fig. 2F). These are canonical cancer cell signaling pathways^{3,35}. In particular, the P53 signaling pathway is well-characterized. The P53 signaling pathway most likely plays a pivotal role in the anti-tumor activity of ginsenosides. Thus, we further explored potential targets *via* PPI analyses. The dysregulated proteins were queried to a dataset for the interacted PPI networks. From the queried and interacted proteins, many were directly enriched and correlated at correlation parameters set to 10, such as GRB2, NFK β , RAS, GSK3 β , PI3K, and TP53 (Fig. 2G). Most of these associated proteins have been shown to be important in cancer cell pathways. In particular, with the correlation parameters increasing to 20 or even more than 30, the TP53 protein (P53) had a superior correlation with the queried dysregulated proteins (Fig. 2H), indicating that it may be one of the positive potential targets in the anti-tumor activity of ginsenosides.

3.3. Integrated miRNA and proteome analyses identified 46 miRNAs that regulate the transcription of 38 proteins that induced by P53

To further elucidate the correlation between the omics of ginsenosides in the A549 cell model, we conducted the miRNA–proteome interaction network analysis of the detected differential miRNA and proteins. Unlike mRNA research, miRNAs provide us with expression-regulation relationships during gene transcriptional translation. In order to keep the entities consistent, we search for theoretical target protein regulatory miRNAs from TargetScanHuman 7.2. As a results, the 73 protein names associated with the proteogenomic analysis were matched with 255 mirbase IDs (Supporting Information Table S2). Then,

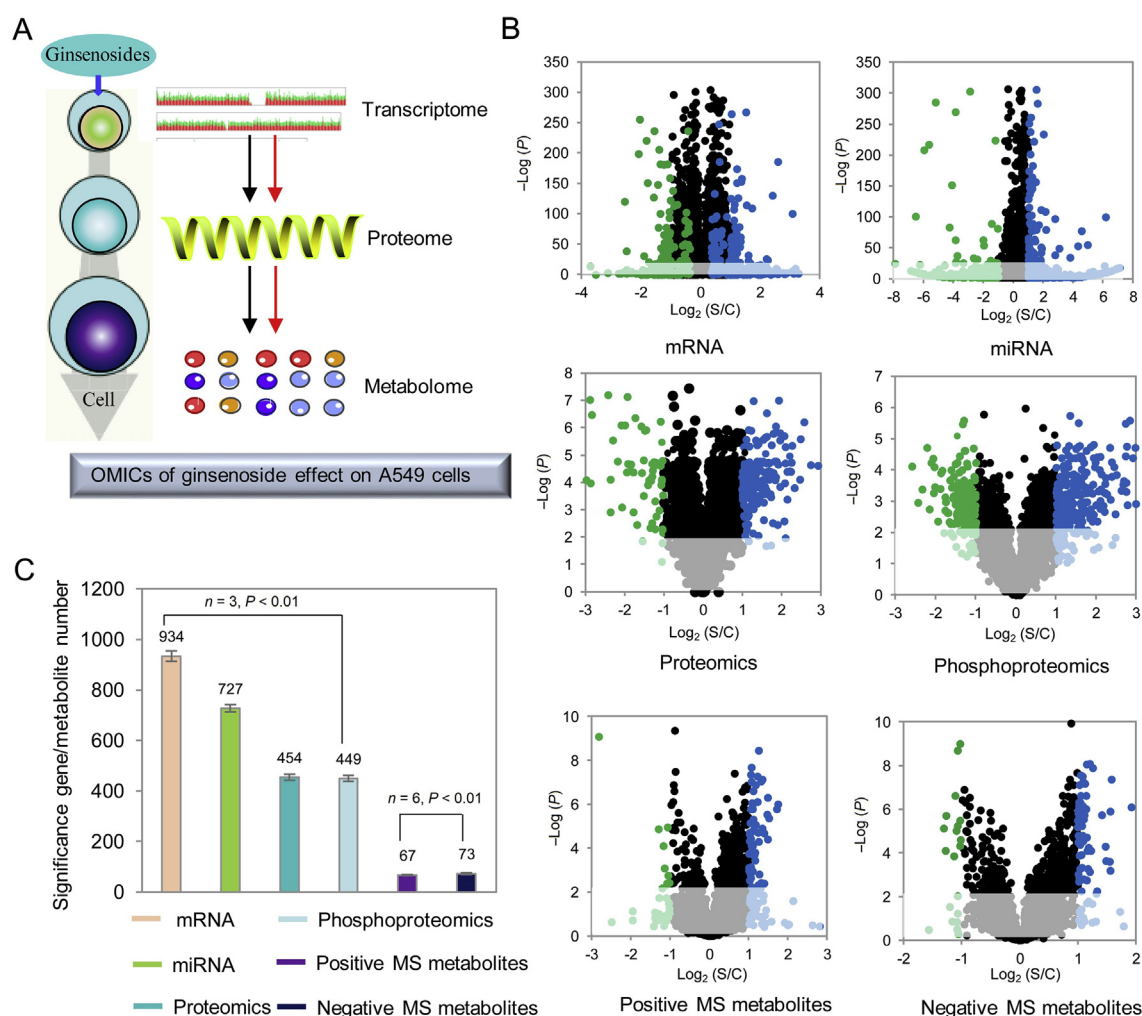


Figure 1 Transcriptome, proteome, and metabolome analyses of the anti-tumor effect of ginsenosides on the non-small cell lung cancer cell line A549. (A) A schematic illustrating the transcriptome, proteome, and metabolome. A549 cells were exposed to ginsenosides or DMSO. (B) Transcriptome (mRNA and miRNA), proteome (proteomics and phosphoproteomics), and metabolome (positive MS metabolites and negative MS metabolites) data were analyzed by volcano plot; x-axis = \log_2 fold change (sample/control), y-axis = $-\log_{10}$ P-value; green circles = downregulated with ginsenoside; blue circles = upregulated with ginsenoside; gray circles = not regulated with ginsenoside. (C) Significant gene, protein, and metabolite numbers. There were 934 regulated mRNAs (P -value < 0.01, $n = 3$), 727 regulated miRNAs (P -value < 0.01, $n = 3$), 454 regulated proteins (P -value < 0.01, $n = 3$), 449 regulated phosphorylated proteins (P -value < 0.01, $n = 3$), 67 regulated positive MS metabolites (P -value < 0.01, $n = 6$), and 73 regulated negative MS metabolites (P -value < 0.01, $n = 6$).

the detected 727 differentially expressed miRNAs were correlated with protein-transformed 255 theoretical miRNAs. The Venn diagram correlation analysis shows that 46 were co-regulated in the miRNA and proteome (Fig. 3A). Moreover, the co-regulated miRNA pathway analysis results were associated with pathways in cancer, including the MAPK, P53, RAS, and PI3K–AKT signaling pathways (Fig. 3B), which was consistent with the previous integrated transcriptome and proteome profiling analysis. The overview of miRNAs and proteins correlation analysis demonstrated apparent mutual regulation in cancer signaling pathways (Supporting Information Fig. S5). In the P53 signaling pathway, most of proteins that were dysregulated according to the proteomic data were also found to have a change in the transcriptome of the corresponding miRNA. These dysregulated proteins and miRNAs control cell survival, apoptosis, angiogenesis inhibition, and many other biological processes within the cancer cell. Additionally, in this study, we found that 46 co-regulated

miRNAs, including hsa-miR-144-3p, hsa-miR-153-3p, hsa-miR-760, hsa-miR-195-5p, hsa-miR-142-5p, hsa-miR-186-5p, hsa-miR-34c-5p, hsa-miR-493-5p, hsa-miR-155-5p, and hsa-miR-485-5p, regulated 38 proteins within the P53 signaling pathway, such as PTEN, IGF, SIVA1, USP8, ATF7IP2, FGFR1, CCND3, TRAF1, RALA, and BCL (Fig. 3C). The association of these miRNAs and proteins not only confirmed the target genes of most of the miRNAs previously reported but also showed that P53 plays a major regulatory role in these changes.

3.4. Integrated proteome and metabolome analysis revealed the anti-tumor activity of ginsenosides regulation nucleotide metabolism, amino acid metabolism and “Warburg effect” through P53

In this study, we integrated the proteome and Metabolome datasets to generate a global and unified view of the anti-tumor activity of

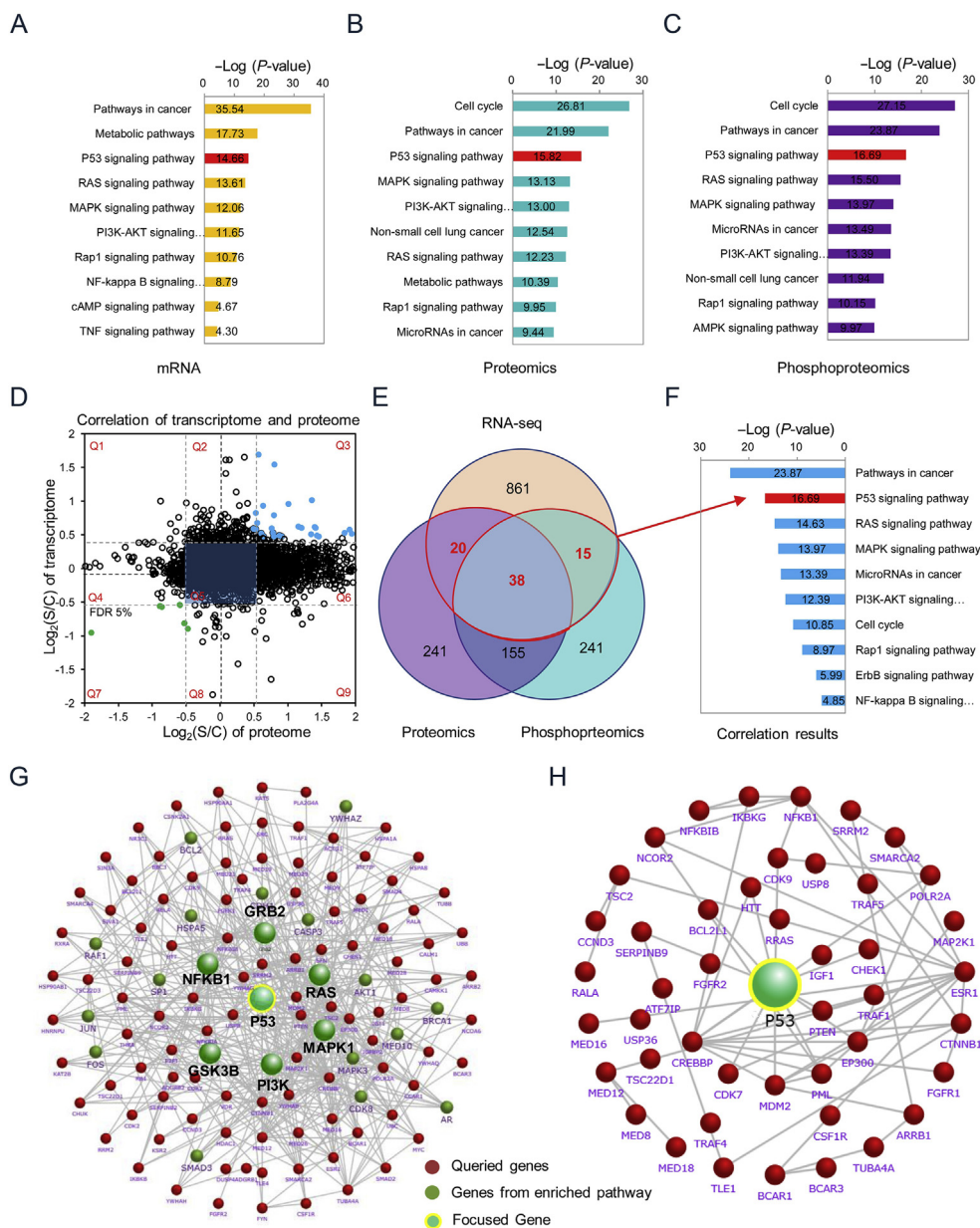


Figure 2 Transcriptome and proteome profiling revealed the functional pathways and critical genes and proteins involved in the anti-tumor activity of ginsenosides. (A) KEGG pathway enrichment of the mRNA data. (B) KEGG pathway enrichment of the proteomics data. (C) KEGG pathway enrichment of the phosphoproteomics data. (D) A nine-quadrant (Q) map of the transcriptome and proteome data correlation analysis. Q5 indicated the co-expressed mRNA and protein that were not differentially expressed. Q3 and 7 indicate the mRNA that was consistent with the corresponding differential expression of proteins. Q1, 2, and 4 indicate the protein expression abundance that was higher than the mRNA. Q6, 8, and 9 indicate protein expression abundance that was lower than the mRNA. Directed P -values are defined as $-\log_{10}(P)$ times the direction of the effect. (E) A Venn diagram showing the overlap of detected genes, proteins, and phosphoproteins. (F) KEGG pathway enrichment of the correlation data. In (A), (B), (C), and (F), the red histograms indicate positive-related pathways. FDR: false discovery rate. (G) Protein-protein interaction (PPI) network models showing interactions among the genes and proteins involved in anti-tumor processes and P53 signaling, which represent top degree subtypes. (H) The regulated genes/proteins (red dots) were directly related to TP53 protein (green dot).

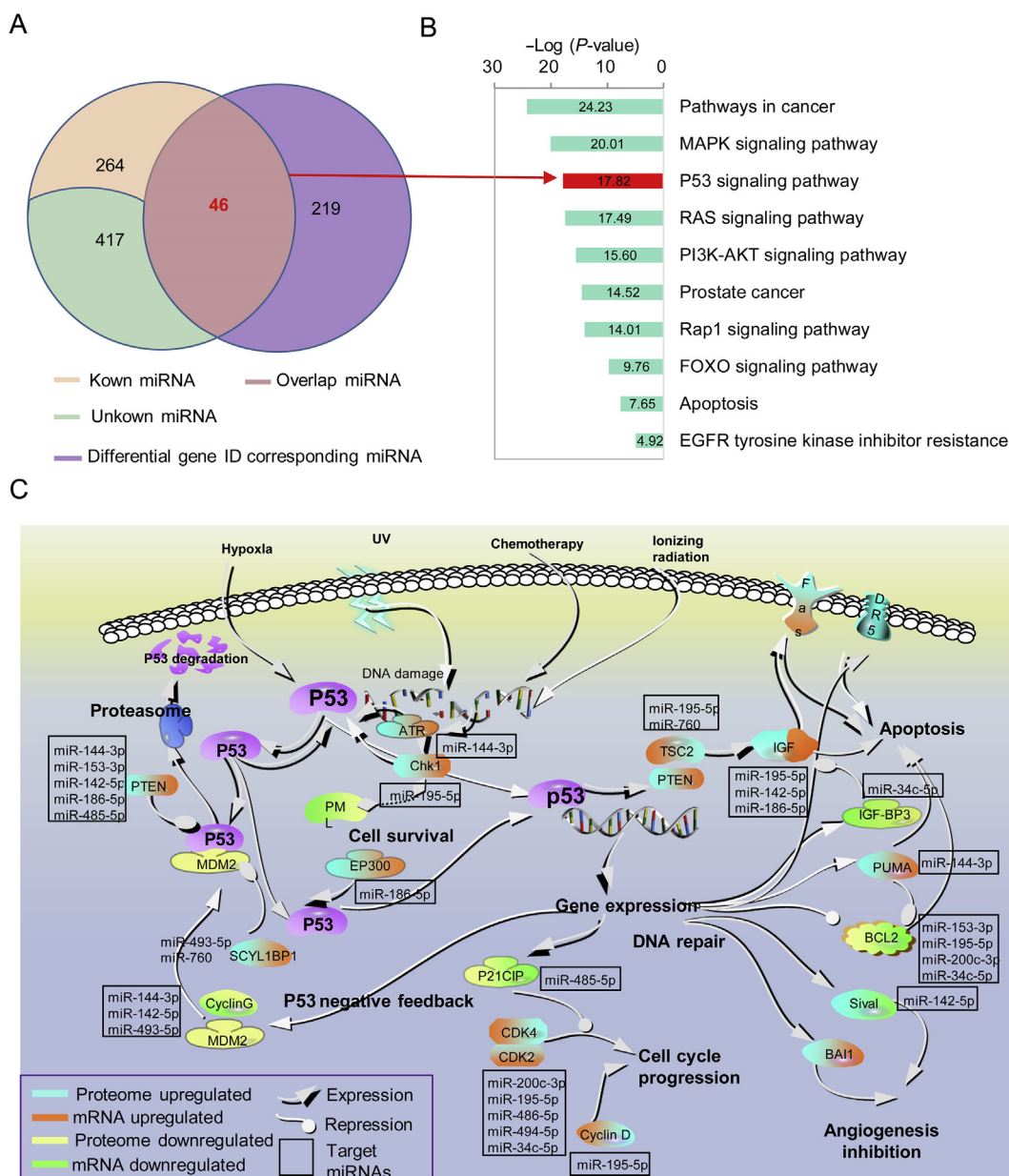


Figure 3 Correlation analysis of the miRNA and proteome data. (A) A Venn diagram showing the overlap of detected miRNA, as well as the corresponding miRNA of differential gene IDs in the transcriptome and proteome correlation analysis. (B) KEGG pathway enrichment in the overlapping miRNAs. Co-regulated miRNA pathway analysis shows that pathways in cancer, MAPK signaling pathway, P53 signaling pathway, RAS signaling pathway, and PI3K–AKT signaling pathway were significantly influenced by treatment with ginsenosides in cancer cells. (C) The P53 signaling pathway showing the various proteins regulated by microRNAs. The dysregulated proteins and miRNAs control cell survival, apoptosis, angiogenesis inhibition, and many other biological processes in cancer cells.

ginsenosides. The significantly changed metabolites are shown in Fig. 4A and Table S1. The KEGG mapping tools were used to integrate the proteome and Metabolome datasets and referenced the human metabolic map (hsa01100, Supporting Information Fig. S6A). The ID mapping and query map are shown in Supporting Information Table S3. The KEGG pathway analysis of the metabolite regulatory proteins demonstrated that the prostate cancer pathway, pathways in cancer, and P53 signaling pathway were the main signaling pathways in the protein–metabolite interaction network underlying the anti-tumor activity of ginsenosides (Fig. 4B). In Fig. 4C, an overview of the gene/protein and

metabolite pathway association analysis map generated based on the significant differential metabolites and gene/proteins. In the gene/protein–metabolite map, each edge representing a metabolic reaction carried out by the proteome (proteomics and phosphoproteomics) that was regulated by ginsenosides. Each node represents a metabolite/protein that changed after treatment with ginsenosides. Proteome and metabolome joint pathway analysis indicated that the edges and nodes were significantly different in nucleotide metabolism, amino acid metabolism, glycolysis, energy metabolism, and metabolism of other amino acids pathways. There is a high rate of amino acid metabolism, nucleotide

metabolism, and glucose consumption in cancer cells, which supports tumor adaptation to metastatic environments and rapid growth³⁶. The rapid occurrence and switch in fuel source demonstrated the important existence of the “Warburg effect” in

the anti-tumor activity of ginsenosides. Moreover, the GO enrichment and functional pathway analysis results demonstrated that alanine, aspartate, and glutamate metabolism, glycerophospholipid metabolism, α -linolenic acid metabolism, and

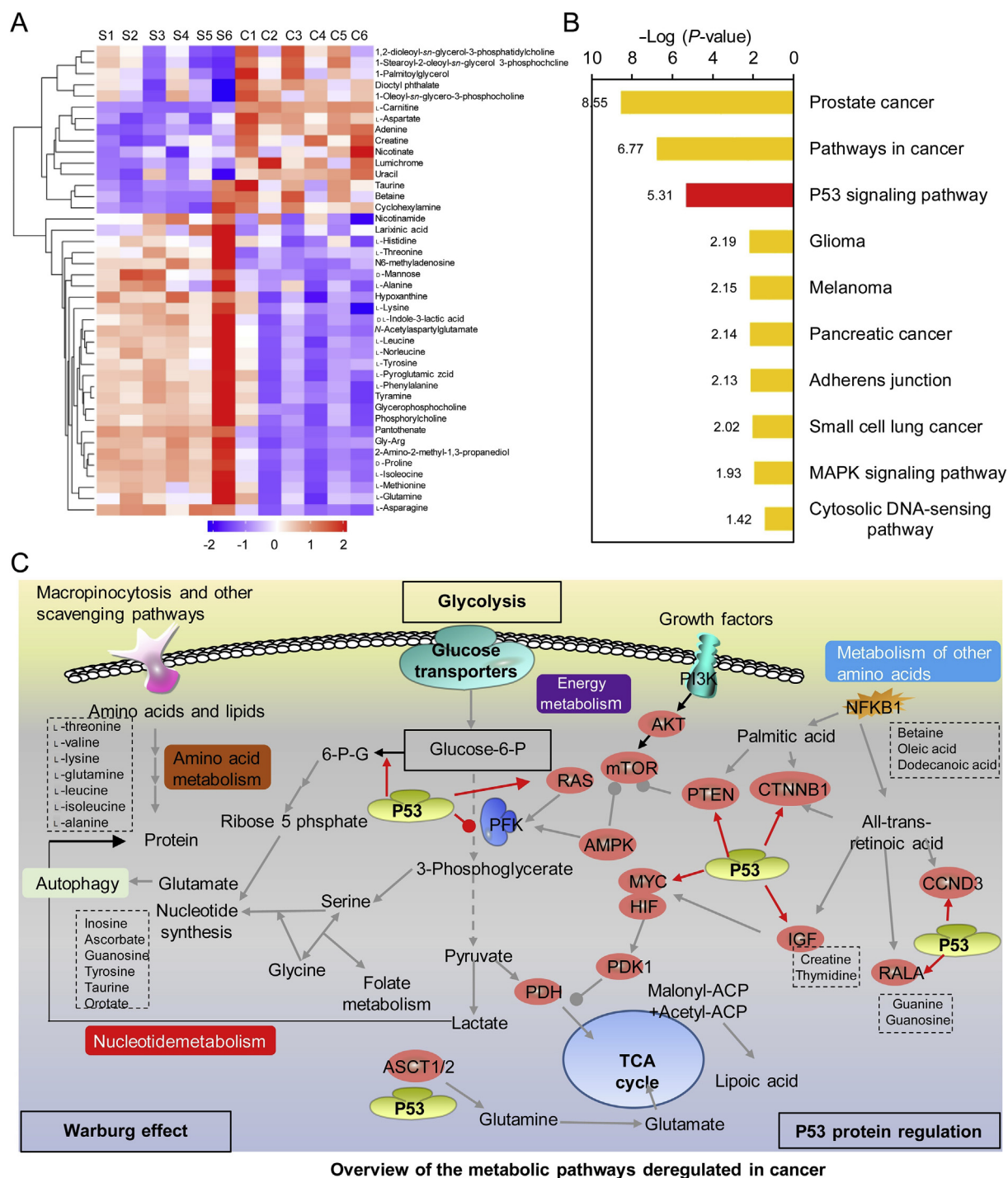


Figure 4 Overview of the joint protein and metabolite pathways involved in the anti-tumor effect of ginsenosides. (A) There were significant differences in the hierarchical clustering results for metabolites. The results show that the metabolites grouped in the same cluster have similar expression patterns and have a relatively close reaction step during the metabolic process. (B) KEGG pathway enrichment of the integrated metabolites and gene interaction network. (C) Overview of the metabolic pathways dysregulated during cancer. Reprogramming of the TCA cycle, glycolysis, and amino acid synthesis occurred in cancer cells treated with ginsenosides, in addition to the associated Warburg effect signaling pathways that directly affect cancer cell metabolism *via* P53 regulation.

arachidonic acid metabolism were all regulated by ginsenosides, as demonstrated in the altered proteomics and phosphoproteomics analysis results (Fig. S6B). These metabolic processes are all common in cancer diseases^{37,38}.

3.5. Multiomics revealed P53 as a key node involved in the anti-tumor network of ginsenosides

In summary, transcriptome and proteome profiling revealed that the antitumor activity of ginsenosides is closely associated with P53; miRNA and proteome analyses identified 46 miRNAs that regulate the transcription of 38 proteins that induced by P53; proteome and Metabolome analysis revealed the anti-tumor activity of ginsenosides regulation nucleotide metabolism, amino acid metabolism and “Warburg effect” through P53. Those transcriptome, proteome, and metabolome profiling highlighted the global changes that occurred after A549 cells were treated with ginsenosides (Fig. 5A). Specifically, the correlation analysis of transcriptome and proteome revealed that the PI3K–AKT signaling pathway, MAPK signaling pathway, RAS signaling pathway, and P53 signaling pathway were all functional pathways involved in the anti-tumor activity of ginsenosides, and the PPI network analysis showed that GRB2, NFK β , RAS, GSK3 β , PI3K, and P53 played a pivotal role in those dysregulated proteins and associated signaling pathways. In particular, P53 had the highest correlation among the queried differentially expressed proteins, indicating that it may be a potential target in the anti-tumor activity of ginsenosides. Additionally, the miRNA–mRNA/proteome interaction network revealed that hsa-miR-144-3p, hsa-miR-153-3p, hsa-miR-760, hsa-miR-195-5p, hsa-miR-142-5p, hsa-miR-186-5p, hsa-miR-34c-5p, hsa-miR-493-5p, hsa-miR-155-5p, and hsa-miR-485-5p regulated 38 proteins within the P53 signaling pathway. The proteome–metabolome interaction network demonstrated obvious protein–metabolite regulation. Furthermore, alanine, aspartate, and glutamate metabolism, glycerophospholipid metabolism, α -linolenic acid metabolism, and arachidonic acid metabolism were all regulated by ginsenosides, as evidenced by the altered proteomics and phosphoproteomics profiles. Our results were consistent with previously published cancer profiles and with the pharmacodynamic mechanism of ginsenosides reported in most previous studies^{39,40}. The final omics GO enrichment and pathway analysis also confirmed these results (Fig. 5B). We summarized the above results in Fig. 5C, which shows that ginsenosides may target to P53 protein, then the genes that bind to the P53 DNA-binding region are affected, and the transcription of these genes is regulated by miRNAs. This ultimately leads to the differential expression of proteins, and the differential expression of these proteins is reflected in a series of cellular signaling pathways, leading to metabolic disorders.

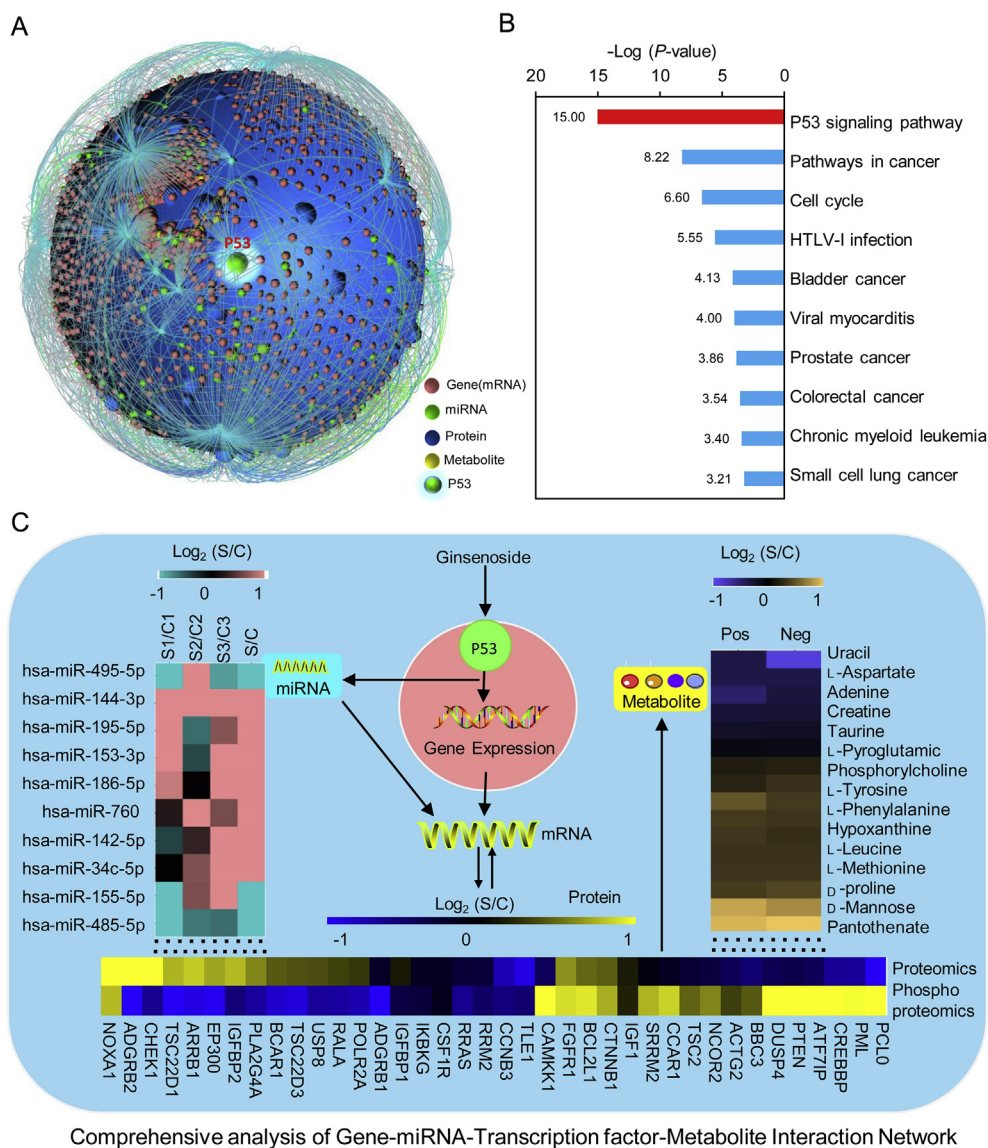
3.6. Identified (*S*)-PPT toward the adjacent regions of the P53 DNA-binding pocket revealed a new target of ginsenosides anti-tumor

In order to ascertain the specific components interacting with the P53 protein, we used affinity MS screening and SPR techniques to screen for the active ligands in ginsenosides and their affinity to target proteins. The recombinant wild-type and mutant P53 proteins (residues 94–312) were purified. Affinity MS screening and SPR fragment library screening were carried out as in previously published articles¹⁹. The affinity index (AI) was used to cut off non-specific binding ligands, where AI > 2, RSD < 30%, and

$P < 0.05$ from three replicates were selected as the initial hits. As a result, 21 compounds from crude ginsenosides showed significant changes in the initial affinity MS screening results (Fig. 6A and Supporting Information Table S4). The SPR fragment library screening was based on a signal response value. When the ligand bound to the protein, the protein attached to the metal chip was warped, thereby causing a change in response signal. However, when the ligand flowed through the metal chip and did not bind to the protein, the response signal did not change. Based on this principle, we identified 15 compounds that were RU > 20, RSD < 30%, and $P < 0.05$ from three replicates (Fig. 6B). We further determined the K_D value of five compounds which were simultaneously screened by comprehensive analysis of the affinity MS screening and the SPR fragment library screening (Supporting Information Fig. S7). The calculated results showed apparent K_D s of 6.628, 10.15, 10.74, 41.11, and 81.04 $\mu\text{mol/L}$ for (*S*)-PPT, 20(*S*)-Ro, 20(*S*)-Rg3, 20(*S*)-PPD, and 20(*S*)-Rh2, respectively, which were all stronger than the known positive P53 protein stabilizer PhiKan083 (122.2 $\mu\text{mol/L}$)⁴¹ (Fig. 6C). These results demonstrated that the ligands we screened from ginsenosides had a high affinity for P53 protein, and (*S*)-PPT had the strongest affinity for P53. Furthermore, the *in silico* docking results suggested that (*S*)-PPT was embedded in the adjacent regions of the P53 DNA-binding pocket, which contained residues V147, D148, T150, P151, Y220, and D228 that coincided with the P53 stabilizer (PhiKan083) binding sites (Fig. 6D). Then we mutated these potential amino acid binding sites individually and purified the recombinant mutant P53 proteins in order to continue the SPR experiment. The calculated K_D s of these mutant P53 proteins with (*S*)-PPT implied that the residues V147, Y220, and D228 obviously influenced the K_D from 6.628 to 246.20 $\mu\text{mol/L}$, 6.628–96.45 $\mu\text{mol/L}$, and 6.628–57.18 $\mu\text{mol/L}$, respectively (Fig. 6E). These results not only confirmed the interaction between the screened ligand and P53 protein but also indicated that (*S*)-PPT directly acted upon the adjacent regions of the P53 DNA-binding pocket and may be able to promote the stability of P53, as well as that of PhiKan 083. Moreover, these key basic residues are highly conserved across not only *Homo sapiens* but also the entire primate family (Fig. 6F). They are reported to play an important role in DNA binding to P53 and transcription.

3.7. (*S*)-PPT targeted P53 and promoted the interaction of P53 with DNA

In order to further confirm that the P53 protein bound to different DNAs and the impact of (*S*)-PPT on the interaction, we first measured the K_D of significance DAN (miR-760 representatives upregulated; miR-493-5p representatives downregulated) and protein by SPR technique. The results showed that both upregulated and downregulated DNAs bound well to proteins, giving a significant K_D value 0.38 $\mu\text{mol/L}$ to miR-760 and 0.10 $\mu\text{mol/L}$ to miR-493-5p (Fig. 7A and B). Then, we designed a fluorescence polarization experiment. The principle of this experiment is that when the DNA with the 5-carboxyfluorescein (5-FAM) label is irradiated by a single plane of polarized light (485 nm), the absorbed light energy jumps into the excited state, then returns to the ground state, and emits a single plane of polarized fluorescence of another wavelength (525 nm). The intensity of the polarized light is positively correlated with the molecular weight of the fluorescent substance. The larger the molecular weight, the slower the rotation, and the more the polarized light is transmitted through the grating. When the DNA and the protein are combined,



Comprehensive analysis of Gene-miRNA-Transcription factor-Metabolite Interaction Network

Figure 5 Global changes in the gene-miRNA-protein-metabolite interaction network involved in the anti-tumor effects of ginsenosides. (A) The general gene-miRNA-protein-metabolite interaction network involved in the anti-tumor effect of ginsenosides. (B) KEGG pathway enrichment of the integrated transcriptome, proteome, and metabolome (co-detected by all three Omics). (C) Ginsenosides targeted P53, which resulted in a series of chain reactions involving genes, mRNAs, proteins, and metabolites. The heat map shows the significant P -values representatives in each omics.

the molecular weight becomes large, and the polarized light signal is enhanced. Specifically, we selected 10 representative miRNAs from the 46 differential miRNAs detected by previous transcriptomics and used them as templates to synthesize DNA fluorescent probes with 5-FAM fluorescent tags, and then detected them separately. The binding efficiency (EC_{50}) represents the strength of probe and protein binding. As a result, 10 of the 5-FAM-labeled DNA probes strongly bound to P53 with an apparent EC_{50} (Fig. 7C and Supporting Information Fig. S8). Furthermore, we conducted drug interference experiments using FAM-DNA (DNA probe based on miRNA-760 and miR-493-5p). Simultaneously fixed DNA probe concentration and the protein concentration, with increased concentrations of (*S*)-PPT, the fluorescence signal becomes much stronger compared with the ligand-free sample (Fig. 7D). These results not only verified the

binding of these miRNAs with DNA with P53 but also indicated that ginsenoside induced (*S*)-PPT, which promoted P53 binding to DNA.

4. Discussion

In this study, we presented a systematic comparative multiomics analysis of the anti-tumor effect of ginsenosides on the non-small cell lung cancer cell line A549. The transcriptome (mRNA and miRNA), proteome (proteomics and phosphoproteomics), and metabolome (positive MS metabolites and negative MS metabolites) flux data identified P53 as a crucial target of ginsenosides. Then, we identified (*S*)-PPT, 20(*S*)-Ro, 20(*S*)-Rg3, 20(*S*)-PPD, and 20(*S*)-Rh2 from ginsenosides through integrated affinity MS screening with SPR fragment library screening

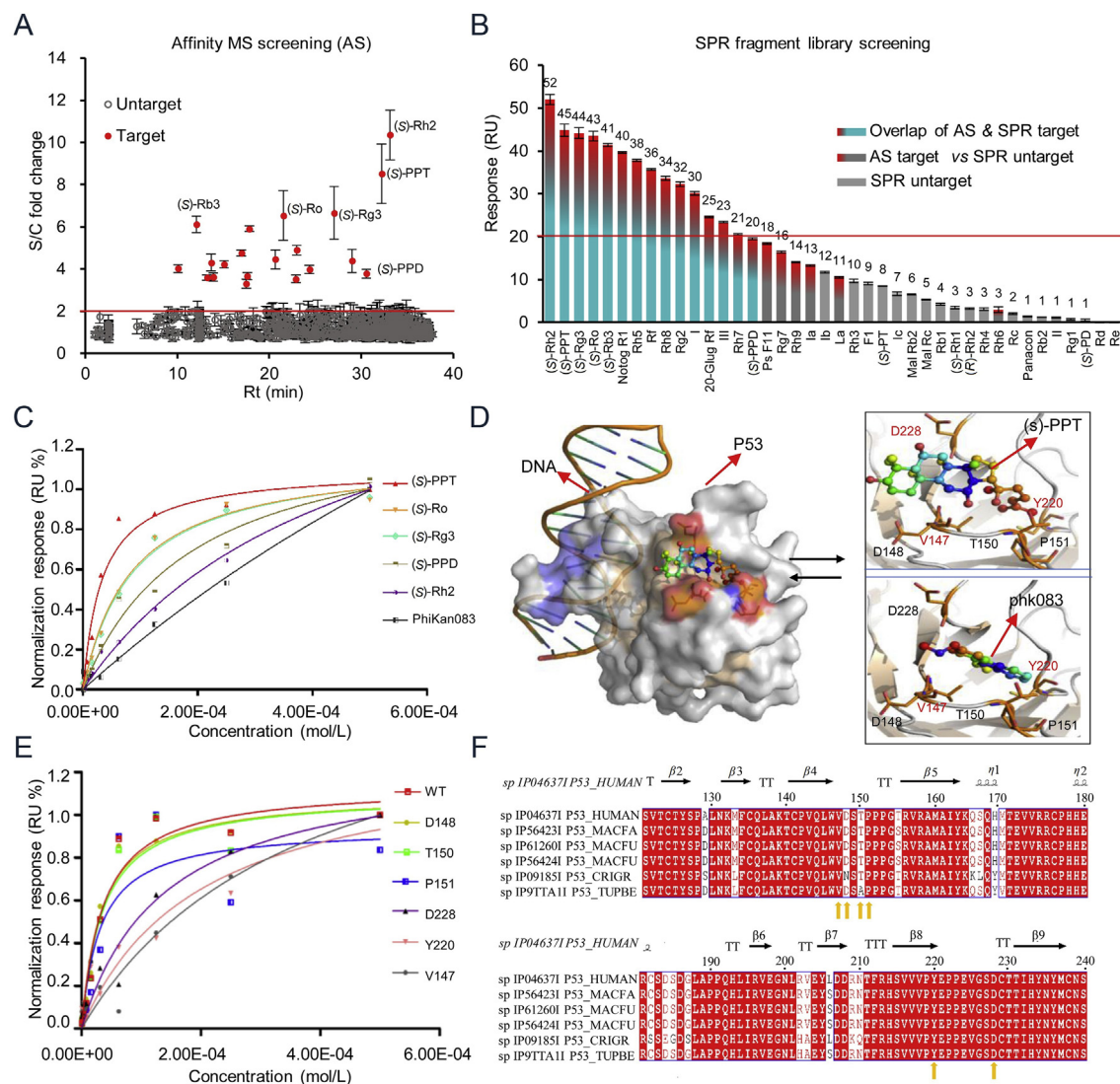


Figure 6 Determination of the target of ginsenosides and the molecular mechanism of the active ingredient of ginsenosides. (A) The affinity MS screening results show that a total of 21 compounds (red points) were significantly changed in the initial affinity MS screening results ($AI > 3$, $n = 3$, $P < 0.05$, and $RSD < 30\%$). (B) The SPR fragment library screening identified 14 compounds which were $RU > 20$, $P < 0.05$, and $RSD < 30\%$ from three replicates (red histogram). (C) The K_D of the identified ligands was calculated by comparing the SPR results with the positive ligand Phikan083. (D) Docking model of (S)-PPT interacting with P53 compared with the crystal ligand PhiKan083 with P53 (PDB code: 4AGL, 6FJ5). (E) The K_D of (S)-PPT with a series of P53 mutant proteins was calculated by SPR. (F) The primary sequence alignment of members of the P53 protein family. Yellow arrows indicate the mutated residue in the binding pockets.

approach as the ligands binding to P53 protein. In particular, (S)-PPT had a lower K_D ($6.628 \mu\text{mol/L}$), and the mutated sites of V147, Y220, and D228 were demonstrated to play a core role in ligand interaction with P53 protein. In addition, by a fluorescence polarization assay, we further confirmed that (S)-PPT promoted the binding function of P53 to DNA and induced a series of omics changes, respectively. The results not only provide a new strategy for us to validation target protein and screening of active ingredients for complex mixtures, but also discover the powerful ingredients for promoting the interaction of P53 with DNA, and driving the therapy of P53 related diseases, especially in anti-tumor.

Identified target protein of compounds has been always a challenge for many researchers^{42,43}. Although there have been many methods for finding target proteins by chemical

modification, these often have high false positive results^{44,45}. In particular, the role of these molecular mechanism in gene transcription, protein translation, protein expression regulation, and metabolic pathways of the overall host cell has not been investigated. Here, by multiomics correlation analysis combine with bioinformatics tools analysis, we found that P53 protein played a general regulatory role in various functional pathways and was probably the direct target protein of a compound in ginsenosides.

Furthermore, we developed a new screening approach that integrated affinity MS screening with SPR fragment library screening in order to identify the active compound in ginsenosides. Obtaining effective compounds from natural products as pro-drugs has become the first choice for current drug development, but the discovery of effective compounds from natural products often involves complex separation and extraction

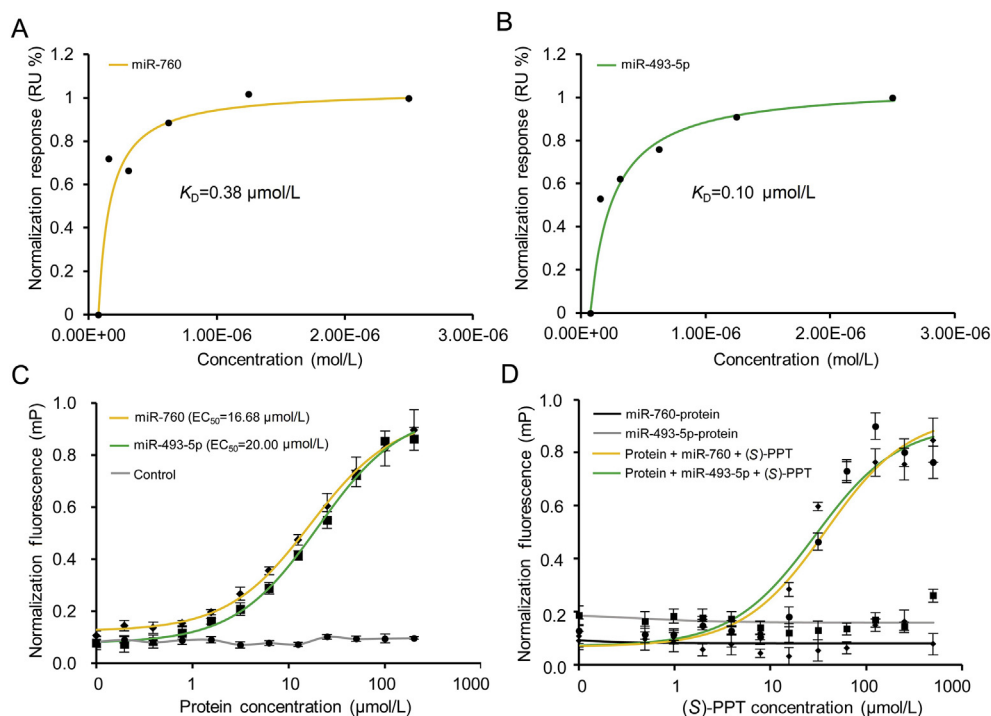


Figure 7 Fluorescence polarization assay revealed (S)-PPT targeted P53 and promoted the integration of P53 with DNA. (A) and (B) The K_D of the upregulated and downregulated DNAs was calculated by SPR. The apparent K_D s were 3.81×10^{-7} mol/L to miR-760 and 1.03×10^{-7} mol/L to miR-493-5p. (C) The potential affinity of different FAM-labeled DNA probes based on the miRNA reverse transcription of P53. Binding efficiency (EC_{50}) was measured by changes in the fluorescence anisotropy of the FAM-DNA with increasing concentrations of protein. (D) The protein (S)-PPT promoted the stability of the interaction of P53 with FAM-labeled DNA. The fluorescence anisotropy of the FAM-DNA changed with increasing (S)-PPT concentrations. The yellow line represents the miR-493-5p binding efficiency enhanced with increasing (S)-PPT concentrations. The green line represents the miR-760 binding efficiency enhanced with increasing (S)-PPT concentrations.

processes, which is time-consuming and labor-intensive^{31,46}. Although we have provided a series of efficient method for screening active compounds from complex systems^{19,31,47}. However, the non-specific binding and the low-screening flux were still an important factor hindering its widespread application in screening drugs. Combining the high throughput of affinity MS with the accuracy of SPR, we can quickly and accurately find effective ligand molecules of target proteins from complex herbal extracts. Based on this principle, we successfully identified (S)-PPT acting on the P53 protein from crude ginsenoside extracts. This provides a new research method for elucidating the target and active ingredients of complex systems.

Finally, we should emphasise that we first discovered that the compound (S)-PPT can promote the binding of P53 to DNA. Various studies have shown that P53 controls a broad and flexible network in transcriptome^{48–50}. As a superior transcription factor, P53 remodeling the miRNA–mRNA interaction network and regulates the expression of several proteins by P53–DNA binding pocket^{51–53}. In this study, by means of molecular docking, protein site mutation and fluorescence polarization assay, we confirmed that the active component of ginsenoside acts on the adjacent regions of the P53 DNA-binding pocket, which promotes the stable binding of P53 with DNA and affects the transcriptional expression of P53-regulated proteins. In particular, in the fluorescence polarization experiment, we designed and synthesized a series of DNA fluorescent probes based on detected differentially expressed miRNAs. Through the combination of these DNA fluorescent probes and proteins, we further confirmed the

mechanism of transcriptional and translational regulation of P53 on these genes. This method determines not only the binding of DNA to protein but also the localization of P53 protein and the screening of P53-interfering RNA drugs.

Data availability

The protein MS data were deposited in iProX⁵⁴ (an official member of ProteomeXchange consortium) as an attachment file (<http://www.iprox.org>) with the project ID IPX0001509000. The sequence read archive accession number for the mRNA data were deposited in NCBI (National Center for Biotechnology Information) as an attachment file with the submission ID SUB5721911 and bioProject ID PRJNA546518. The sequence read archive accession number for the microRNA data were deposited in NCBI as an attachment file (<http://www.ncbi.nlm.nih.gov/bioproject/546520>) with the submission ID SUB5733948 and bioProject ID PRJNA546520. The metabolomics data reported in this paper were deposited in Metabolomics Workbench⁵⁵ as an attachment file (<https://doi.org/10.21228/M8WD6C>) with the Project ID PR000803 and study ID ST001191.

Acknowledgments

This research was supported by International Cooperation and Exchange of the National Natural Science Foundation of China (No. 81761168039), Macau Science and Technology

Development 345 Fund (No. 015/2017/AFJ, China), and National Key Research and Development Program of China (Nos. 2018YFC1704800 and 2018YFC1704805).

Author contributions

Gang Bai, Zhihong Jiang, Yuanyuan Hou and Zhihua Wang designed the study. Zhihua Wang performed experiments, acquired and analyzed data. B.W, C.G, and Y.G assisted with SPR experiments. Chaowen Li, Ruixue Niu and Min Jiang assisted with cell experiments. Zhihua Wang, Liping Bai, Elaine Laihan Leung, Jie Gao and Yuanyuan Hou analyzed and interpreted data. Gang Bai, Yuanyuan Hou and Zhihong Jiang contributed to completing the revision and submission of the article. All authors approved the content of the manuscript.

Conflicts of interest

The authors declare no conflicts of interest.

Appendix A. Supporting information

Supporting data to this article can be found online at <https://doi.org/10.1016/j.apsb.2020.01.017>.

References

- Kastenhuber ER, Lowe SW. Putting P53 in context. *Cell* 2017;**170**:1062–78.
- Yu ZY, Wu FL, Chen L, Li Q, Wang CJ, Dong JH, et al. ETME, a novel beta-element derivative, synergizes with arsenic trioxide in inducing apoptosis and cell cycle arrest in hepatocarcinoma cells via a P53-dependent pathway. *Acta Pharm Sin B* 2014;**4**:424–9.
- Kotler E, Shani O, Goldfeld G, Lotan-Pompan M, Tarcic O, Gershoni A, et al. A systematic P53 mutation library links differential functional impact to cancer mutation pattern and evolutionary conservation. *Mol Cell* 2018;**71**:178–190. e8.
- Mello SS, Valente LJ, Raj N, Seoane JA, Flowers BM, McClendon J, et al. A P53 super-tumor suppressor reveals a tumor suppressive P53-Ptpn14-Yap axis in pancreatic cancer. *Cancer Cell* 2017;**32**:460–473. e6.
- Krell J, Stebbing J, Frampton AE, Carissimi C, Harding V, de Giorgio A, et al. The role of TP53 in miRNA loading onto AGO2 and in remodelling the miRNA–mRNA interaction network. *Lancet* 2015;**385**(Suppl. 1):S15.
- Li L, Wu J, Sima X, Bai P, Deng W, Deng X, et al. Interactions of miR-34b/c and TP-53 polymorphisms on the risk of nasopharyngeal carcinoma. *Tumour Biol* 2013;**34**:1919–23.
- Salvoza NC, Klinzing DC, Gopez-Cervantes J, Baclig MO. Association of circulating serum miR-34a and miR-122 with dyslipidemia among patients with non-alcoholic fatty liver disease. *PLoS One* 2016;**11**:e0153497.
- Jain AK, Barton MC. Outside the P53 RING: transcription regulation by chromatin-bound MDM2. *Mol Cell* 2016;**62**:805–7.
- Marques-Torres MA, Porlan E, Banito A, Gomez-Ibarlucea E, Lopez-Contreras AJ, Fernandez-Capetillo O, et al. Cyclin-dependent kinase inhibitor p21 controls adult neural stem cell expansion by regulating Sox2 gene expression. *Cell Stem Cell* 2013;**12**:88–100.
- Pan R, Ruvolo V, Mu H, Levenson JD, Nichols G, Reed JC, et al. Synthetic lethality of combined BCL-2 inhibition and P53 activation in AML: mechanisms and superior antileukemic efficacy. *Cancer Cell* 2017;**32**:748–760. e6.
- Wang L, Xiong H, Wu F, Zhang Y, Wang J, Zhao L, et al. Hexokinase 2-mediated Warburg effect is required for PTEN- and P53-deficiency-driven prostate cancer growth. *Cell Rep* 2014;**8**:1461–74.
- Johnson RF, Perkins ND. Nuclear factor-kappaB, P53, and mitochondria: regulation of cellular metabolism and the Warburg effect. *Trends Biochem Sci* 2012;**37**:317–24.
- Fenoglio-Preiser CM, Wang J, Stemmermann GN, Noffsinger A. TP53 and gastric carcinoma: a review. *Hum Mutat* 2003;**21**:258–70.
- Low TY, van Heesch S, van den Toorn H, Giansanti P, Cristobal A, Toonen P, et al. Quantitative and qualitative proteome characteristics extracted from in-depth integrated genomics and proteomics analysis. *Cell Rep* 2013;**5**:1469–78.
- Verstraeten SL, Albert M, Paquot A, Muccioli GG, Tyteca D, Mingot-Leclercq MP. Membrane cholesterol delays cellular apoptosis induced by ginsenoside Rh2, a steroid saponin. *Toxicol Appl Pharmacol* 2018;**352**:59–67.
- Wang XJ, Zhou RJ, Zhang N, Jing Z. 20(S)-Ginsenoside Rg3 sensitizes human non-small cell lung cancer cells to icotinib through inhibition of autophagy. *Eur J Pharmacol* 2019;**850**:141–9.
- Lin MB, Sun W, Gong W, Ding YS, Zhuang YY, Hou Q. Ginsenoside Rg1 protects against transient focal cerebral ischemic injury and suppresses its systemic metabolic changes in cerebral injury rats. *Acta Pharm Sin B* 2015;**5**:277–84.
- He CY, Feng R, Sun YP, Chu SF, Chen J, Ma C, et al. Simultaneous quantification of ginsenoside Rg1 and its metabolites by HPLC–MS/MS: Rg1 excretion in rat bile, urine and feces. *Acta Pharm Sin B* 2016;**6**:593–9.
- Wang Z, Kim U, Jiao Y, Li C, Guo Y, Ma X, et al. Quantitative proteomics combined with affinity MS revealed the molecular mechanism of ginsenoside antitumor effects. *J Proteome Res* 2019;**18**:2100–8.
- Paraskevopoulou MD, Georgakilas G, Kostoulas N, Vlachos IS, Vergoulis T, Reczko M, et al. DIANA-microT web server v5.0: service integration into miRNA functional analysis workflows. *Nucleic Acids Res* 2013;**41**:W169–73.
- Bindea G, Mlecnik B, Hackl H, Charoentong P, Tosolini M, Kirilovsky A, et al. ClueGO: a Cytoscape plug-in to decipher functionally grouped gene ontology and pathway annotation networks. *Bioinformatics* 2009;**25**:1091–3.
- McDowall MD, Scott MS, Barton GJ. PIPs: human protein–protein interaction prediction database. *Nucleic Acids Res* 2009;**37**:D651–6.
- Szklarczyk D, Gable AL, Lyon D, Junge A, Wyder S, Huerta-Cepas J, et al. STRING v11: protein–protein association networks with increased coverage, supporting functional discovery in genome-wide experimental datasets. *Nucleic Acids Res* 2019;**47**:D607–13.
- Zhou G, Xia J. OmicsNet: a web-based tool for creation and visual analysis of biological networks in 3D space. *Nucleic Acids Res* 2018;**46**:W514–22.
- Shannon P, Markiel A, Ozier O, Baliga NS, Wang JT, Ramage D, et al. Cytoscape: a software environment for integrated models of biomolecular interaction networks. *Genome Res* 2003;**13**:2498–504.
- Agarwal V, Bell GW, Nam JW, Bartel DP. Predicting effective microRNA target sites in mammalian mRNAs. *Elife* 2015;**4**:e05005.
- Chong J, Yamamoto M, Xia J. MetaboAnalystR 2.0: from raw spectra to biological insights. *Metabolites* 2019;**9**:57.
- Bullock AN, Henckel J, DeDecker BS, Johnson CM, Nikolova PV, Proctor MR, et al. Thermodynamic stability of wild-type and mutant P53 core domain. *Proc Natl Acad Sci U S A* 1997;**94**:14338–42.
- Joerger AC, Ang HC, Veprincev DB, Blair CM, Fersht AR. Structures of P53 cancer mutants and mechanism of rescue by second-site suppressor mutations. *J Biol Chem* 2005;**280**:16030–7.
- Fu X, Wang Z, Li L, Dong S, Li Z, Jiang Z, et al. Novel chemical ligands to ebola virus and marburg virus nucleoproteins identified by combining affinity mass spectrometry and metabolomics approaches. *Sci Rep* 2016;**6**:29680.
- Wang Z, Kim U, Liu J, Cheng C, Wu W, Guo S, et al. Comprehensive TCM molecular networking based on MS/MS *in silico* spectra with integration of virtual screening and affinity MS screening for discovering functional ligands from natural herbs. *Anal Bioanal Chem* 2019;**411**:5785–97.

32. Golovenko D, Brauning B, Vyas P, Haran TE, Rozenberg H, Shakked Z. New insights into the role of DNA shape on its recognition by P53 proteins. *Structure* 2018;**26**:1237–1250. e6.
33. Halgren TA, Murphy RB, Friesner RA, Beard HS, Frye LL, Pollard WT, et al. Glide: a new approach for rapid, accurate docking and scoring. 2. Enrichment factors in database screening. *J Med Chem* 2004;**47**:1750–9.
34. Robert X, Gouet P. Deciphering key features in protein structures with the new ENDscript server. *Nucleic Acids Res* 2014;**42**:W320–4.
35. Kowalski JR, Bhaduri A, Zehnder AM, Neela PH, Che Y, Wozniak GG, et al. The functional proximal proteome of oncogenic Ras includes mTORC2. *Mol Cell* 2019;**73**:830–44. e12.
36. Schell JC, Olson KA, Jiang L, Hawkins AJ, Van Vranken JG, Xie J, et al. A role for the mitochondrial pyruvate carrier as a repressor of the Warburg effect and colon cancer cell growth. *Mol Cell* 2014;**56**:400–13.
37. Maddocks OD, Labuschagne CF, Adams PD, Vousden KH. Serine metabolism supports the methionine cycle and DNA/RNA methylation through *de novo* ATP synthesis in cancer cells. *Mol Cell* 2016;**61**:210–21.
38. Ferrer CM, Lynch TP, Sodi VL, Falcone JN, Schwab LP, Peacock DL, et al. O-GlcNAcylation regulates cancer metabolism and survival stress signaling via regulation of the HIF-1 pathway. *Mol Cell* 2014;**54**:820–31.
39. Donohoe DR, Collins LB, Wali A, Bigler R, Sun W, Bultman SJ. The Warburg effect dictates the mechanism of butyrate-mediated histone acetylation and cell proliferation. *Mol Cell* 2012;**48**:612–26.
40. Sodrul IMD, Wang C, Chen X, Du J, Sun H. Role of ginsenosides in reactive oxygen species-mediated anticancer therapy. *Oncotarget* 2018;**9**:2931–50.
41. Baud MGJ, Bauer MR, Verduci L, Dingler FA, Patel KJ, Horil Roy D, et al. Aminobenzothiazole derivatives stabilize the thermolabile P53 cancer mutant Y220C and show anticancer activity in P53-Y220C cell lines. *Eur J Med Chem* 2018;**152**:101–14.
42. Zhang Y, Wang ZH, Ma XY, Yang SN, Hu XY, Tao J, et al. Glycyrrhetic acid binds to the conserved P-loop region and interferes with the interaction of RAS-effector proteins. *Acta Pharm Sin B* 2019;**9**:294–303.
43. Wang WW, Liu C, Zhu NY, Lin Y, Jiang JD, Wang YC, et al. Identification of anti-Gram-negative bacteria agents targeting the interaction between ribosomal proteins L12 and L10. *Acta Pharm Sin B* 2018;**8**:772–83.
44. Yang SN, Zhang Y, Shen FK, Ma XY, Zhang M, Hou YY, et al. The flavonoid baicalin improves glucose metabolism by targeting the PH domain of AKT and activating AKT/GSK3 beta phosphorylation. *FEBS Lett* 2019;**593**:175–86.
45. Ma X, Zhang Y, Wang Z, Shen Y, Zhang M, Nie Q, et al. Ursolic acid, a natural nutraceutical agent, targets caspase3 and alleviates inflammation-associated downstream signal transduction. *Mol Nutr Food Res* 2017;**61**:1700332.
46. Han X, Jiang H, Han L, Xiong X, He YN, Fu CM, et al. A novel quantified bitterness evaluation model for traditional Chinese herbs based on an animal ethology principle. *Acta Pharm Sin B* 2018;**8**:209–17.
47. Wang Z, Liang H, Cao H, Zhang B, Li J, Wang W, et al. Efficient ligand discovery from natural herbs by integrating virtual screening, affinity mass spectrometry and targeted metabolomics. *Analyst* 2019;**144**:2881–90.
48. Sorenson EC, Khanin R, Bamboat ZM, Cavnar MJ, Kim TS, Sadot E, et al. Genome and transcriptome profiling of fibrolamellar hepatocellular carcinoma demonstrates P53 and IGF2BP1 dysregulation. *PLoS One* 2017;**12**:e0176562.
49. Wang B, Niu D, Lam TH, Xiao Z, Ren EC. Mapping the P53 transcriptome universe using P53 natural polymorphs. *Cell Death Differ* 2014;**21**:521–32.
50. Vig S, Talwar P, Kaur K, Srivastava R, Srivastava AK, Datta M. Transcriptome profiling identifies P53 as a key player during calreticulin deficiency: implications in lipid accumulation. *Cell Cycle* 2015;**14**:2274–84.
51. Jones J, Faustino V, Nogaj L. Cloning the P53 DNA binding domain. *Faseb J* 2018;**32**:892–6638.
52. He F, Borchers W, Song TJ, Wei X, Das M, Chen LH, et al. Interaction between P53 N terminus and core domain regulates specific and nonspecific DNA binding. *Proc Natl Acad Sci U S A* 2019;**116**:8859–68.
53. Pradhan MR, Siau JW, Kannan S, Nguyen MN, Ouaray Z, Kwok CK, et al. Simulations of mutant P53 DNA binding domains reveal a novel druggable pocket. *Nucleic Acids Res* 2019;**47**:1637–52.
54. Ma J, Chen T, Wu S, Yang C, Bai M, Shu K, et al. iProX: an integrated proteome resource. *Nucleic Acids Res* 2019;**47**:D1211–7.
55. Sud M, Fahy E, Cotter D, Azam K, Vadivelu I, Burant C, et al. Metabolomics Workbench: an international repository for metabolomics data and metadata, metabolite standards, protocols, tutorials and training, and analysis tools. *Nucleic Acids Res* 2016;**44**:D463–70.